



The effect of radiative feedback on disc fragmentation

Anthony Mercer[★] and Dimitris Stamatellos

Jeremiah Horrocks Institute for Mathematics, Physics & Astronomy, University of Central Lancashire, Preston PR1 2HE, UK

Accepted 2016 October 19. Received 2016 October 14; in original form 2016 June 1

ABSTRACT

Protostellar discs may become massive enough to fragment producing secondary low-mass objects: planets, brown dwarfs and low-mass stars. We study the effect of radiative feedback from such newly formed secondary objects using radiative hydrodynamic simulations. We compare the results of simulations without any radiative feedback from secondary objects with those where two types of radiative feedback are considered: (i) continuous and (ii) episodic. We find that (i) continuous radiative feedback stabilizes the disc and suppresses further fragmentation, reducing the number of secondary objects formed; (ii) episodic feedback from secondary objects heats and stabilizes the disc when the outburst occurs, but shortly after the outburst stops, the disc becomes unstable and fragments again. However, fewer secondary objects are formed compared to the case without radiative feedback. We also find that the mass growth of secondary objects is mildly suppressed due to the effect of their radiative feedback. However, their mass growth also depends on where they form in the disc and on their subsequent interactions, such that their final masses are not drastically different from the case without radiative feedback. We find that the masses of secondary objects formed by disc fragmentation are from a few M_J to a few $0.1 M_\odot$. Planets formed by fragmentation tend to be ejected from the disc. We conclude that planetary-mass objects on wide orbits (wide-orbit planets) are unlikely to form by disc fragmentation. Nevertheless, disc fragmentation may be a significant source of free-floating planets and brown dwarfs.

Key words: methods: numerical – planet–disc interactions – protoplanetary discs – brown dwarfs.

1 INTRODUCTION

Stars form from the gravitational collapse of dense cores within turbulent molecular clouds. Due to turbulence and/or the initial rotation of these cores, newly formed stars are attended by protostellar discs of gas and dust (e.g. Terebey, Shu & Cassen 1984; Attwood et al. 2009). The idea that our Solar system formed from a protostellar disc has been discussed since the 18th century (Laplace 1796). We now know that discs play a fundamental role in the formation of stars and planets. They provide young stars with the majority of their mass through accretion and a suitable dynamical and chemical environment for the formation of planets (e.g. Lissauer 1993).

Mass accretion on to young stars increases their luminosity due to gravitational energy being converted into heat on the accretion shock around the surface of a star. The accretion is typically considered to be continuous (Krumholz 2006; Bate 2009; Offner et al. 2009; Krumholz & Burkert 2010). However, consider a star which has just evolved out of the Class 0 phase, which will ultimately have a mass of $1M_\odot$. It has an age of $\sim 10^5$ yr and has accumulated half of its final

mass. This yields a mean mass accretion rate of $\sim 5 \times 10^{-6} M_\odot \text{yr}^{-1}$ and a mean luminosity of $\sim 25 L_\odot$. Observational studies show that solar-like protostars have much lower luminosities (e.g. Kenyon et al. 1990; Enoch et al. 2009; Evans et al. 2009). This is the so-called *luminosity problem*. It may be circumvented if accretion on to protostars is not continuous, but rather episodic, happening in short bursts (e.g. Dunham et al. 2010; Dunham & Vorobyov 2012; Audard et al. 2014).

FU Ori objects provide evidence of episodic accretion. These objects exhibit sudden luminosity increases of the order of ~ 5 mag and estimated accretion rates of $> 10^{-4} M_\odot \text{yr}^{-1}$ which last from a few tens of years to a few centuries (Herbig 1977; Hartmann & Kenyon 1996; Greene, Aspin & Reipurth 2008; Peneva et al. 2010; Green et al. 2011).

Episodic accretion may be due to gravitational instabilities (Vorobyov & Basu 2005; Machida, Inutsuka & Matsumoto 2011; Vorobyov & Basu 2015; Liu et al. 2016), thermal instabilities in the inner disc region (Hartmann & Kenyon 1985; Lin, Faulkner & Papaloizou 1985; Bell & Lin 1994), or gravitational interactions in a binary system (Bonnell & Bastien 1992; Forgan & Rice 2010). It has also been suggested that they may be due to the combined effect of gravitational instabilities operating in the outer disc region

* E-mail: apmercer@uclan.ac.uk.

transferring matter inwards and the magnetorotational instability (MRI) operating episodically in the inner disc region delivering matter on to the young protostar (Armitage, Livio & Pringle 2001; Zhu et al. 2007; Zhu, Hartmann & Gammie 2009a; Zhu et al. 2009b, 2010).

It is expected that radiative feedback from young protostars will affect the dynamical and thermal evolution of their parent cloud and their discs (Stamatellos, Whitworth & Hubber 2011b, 2012; Lomax et al. 2014; Guszejnov, Krumholz & Hopkins 2016). A significant fraction of low-mass stars and brown dwarfs may form by fragmentation in gravitationally unstable discs (Whitworth & Stamatellos 2006; Stamatellos, Hubber & Whitworth 2007a; Stamatellos & Whitworth 2009a; Kratter et al. 2010a; Zhu et al. 2012; Vorobyov 2013; Lomax et al. 2014; Kratter & Lodato 2016). Protostellar discs fragment if two conditions are met. (i) They are gravitationally unstable i.e.

$$Q \equiv \frac{\kappa c_s}{\pi G \Sigma} < \beta, \quad (1)$$

where Q is the Toomre parameter (Toomre 1964), κ is the epicyclic frequency, c_s is the local sound speed and Σ is the disc surface density. The value of β is of the order of unity and it is dependent on the assumed geometry of the disc and the equation of state used: for a razor-thin disc, $\beta = 1$; in a 3D disc $\beta = 1.4$ (see Durisen et al. 2007, and references therein). (ii) They cool sufficiently fast, i.e. $t_{\text{COOL}} < (0.5-2)t_{\text{ORB}}$, where t_{ORB} is the local orbital period (Gammie 2001; Johnson & Gammie 2003; Rice et al. 2003b; Rice, Lodato & Armitage 2005). In the last few years, the validity of second criterion has been scrutinized, and it has been suggested that fragmentation may happen for even slower cooling rates (Lodato & Clarke 2011; Meru & Bate 2011; Paardekooper, Baruteau & Meru 2011; Rice, Forgan & Armitage 2012; Tsukamoto et al. 2015). However, irrespective of the detailed criteria, there has been significant observational evidence that disc fragmentation does occur (Tobin et al. 2013, 2016; Dupuy et al. 2016).

Theoretical work and numerical simulations suggest that the conditions for disc fragmentation are met in the outer disc regions ($>70-100$ au; e.g. Whitworth & Stamatellos 2006; Stamatellos & Whitworth 2008, 2009b; Boley 2009; Stamatellos et al. 2011a). Most of the objects formed by disc fragmentation are brown dwarfs, though low-mass stars and planets may also form (Stamatellos & Whitworth 2009a; Zhu et al. 2012; Vorobyov 2013). Fragments that form in gravitationally unstable discs start off with a mass that is determined by the opacity limit for fragmentation, i.e. with a few M_J , where M_J is the mass of Jupiter (Low & Lynden-Bell 1976; Rees 1976; Boss 1988; Whitworth & Stamatellos 2006; Boley et al. 2010; Forgan & Rice 2011; Rogers & Wadsley 2012). However, they quickly accrete mass to become brown dwarfs or even low-mass stars (Stamatellos & Whitworth 2009a; Kratter, Murray-Clay & Youdin 2010b; Zhu et al. 2012; Stamatellos 2015). A few of the fragments remain in the planetary-mass regime ($M < 13 M_J$) but these are typically ejected from the disc (Li et al. 2015, 2016) becoming free-floating planets (e.g. Zapatero-Osorio et al. 2000; Kellogg et al. 2016).

These low-mass objects that form by disc fragmentation have properties that are similar to the properties of objects forming from the collapse of isolated low-mass pre-(sub)stellar cloud cores. They are expected to be attended by discs (Stamatellos & Whitworth 2009a; Liu et al. 2015; Sallum et al. 2015), and they may also launch jets perpendicular to the disc axis (Machida, Inutsuka & Matsumoto 2006; Gressel et al. 2015). Stamatellos & Herczeg (2015) suggest that discs around low-mass objects (brown dwarfs

and planets) that form by disc fragmentation are more massive from what would be expected if they were formed in collapsing low-mass pre-(sub)stellar cloud cores, which is consistent with recent observations of brown dwarf discs in Upper Sco OB1 and Ophiuchus (van der Plas et al. 2016).

It is therefore reasonable to assume that low-mass objects that form by disc fragmentation may also exhibit radiative feedback due to accretion of material from their individual discs on to their surfaces. The effect of radiative feedback due to accretion on to low-mass objects such as planets and brown dwarfs has been ignored by previous studies of disc fragmentation. Recent simulations of the evolution of giant protoplanets in self-gravitating discs (Stamatellos 2015) have shown that radiative feedback from giant planets may reduce gas accretion and hence suppress their mass growth. They found that when radiative feedback is included, the fragment's final mass is within the planetary-mass regime (see also Nayakshin & Cha 2013).

The goal of this paper is to examine how radiative feedback from objects that form by disc fragmentation influences the properties of these objects and whether subsequent fragmentation in the disc is affected. More specifically, we investigate whether radiative feedback from objects forming in the disc (hereafter referred to as *secondary objects*) suppresses their mass growth, increasing the possibility that these objects will end up as planets rather than brown dwarfs of more massive objects, in contrast with what previous studies suggest (e.g. Stamatellos & Whitworth 2009a; Kratter et al. 2010b).

We construct numerical experiments to examine three cases of radiative feedback from secondary objects. (i) No radiative feedback (NRF): gas is accreted on to the objects but no energy is fed back into the disc due to this process. (ii) Continuous radiative feedback (CRF): gas is accreted continuously on to the object and the accretion energy is continuously fed back into the disc. (iii) Episodic radiative feedback (ERF): we assume that low-mass secondary objects exhibit episodic outbursts just like their higher mass counterparts do. Gas accumulates into the region close to the object (within ~ 1 au) and when the conditions are right, it accretes on to the object (see Section 2 for details). Gas accretion on to secondary objects is episodic, resulting in ERF.

In Section 2, we provide the computational framework of this work including the episodic accretion/feedback model we adopt. In Section 3, we discuss the initial conditions of the simulations. We present the results of the effect of radiative feedback on the evolution of discs and on the properties of the objects form by disc fragmentation in Section 4. Our results are summarized in Section 5.

2 NUMERICAL METHOD

We use the smoothed particle hydrodynamics (SPH) code SEREN (Hubber et al. 2011a,b) to simulate gravitationally unstable protostellar discs. Discs are represented by a large number of SPH particles. To avoid small timesteps at a density of $\rho_{\text{sink}} = 10^{-9}$ g cm $^{-3}$, a particle is replaced by a sink (Bate, Bonnell & Price 1995) that represents a bound object (star, brown dwarf or planet, depending on its mass). Sinks interact with the rest of the disc both gravitationally and radiatively (in the cases where radiative feedback is included). Gas particles which pass within $R_{\text{sink}} = 1$ au and are gravitationally bound to a sink are accreted on to it.

The heating and cooling of gas are performed using the radiative transfer technique ascribed to Stamatellos et al. (2007b), where the density and the gravitational potential of a gas particle are used to estimate a column density through which cooling/heating happens, and along with the local opacity, are used to estimate an optical depth

for each particle. This can be used to determine the heating and cooling of the particle and incorporates effects from the rotational and vibrational degrees of freedom of H₂, the dissociation of H₂, ice melting, dust sublimation, bound-free, free-free and electron scattering interactions. The equation of state used and the effect of each assumed constituent are described in detail in section 3 of Stamatellos et al. (2007b). The radiative heating/cooling rate of a particle i is

$$\frac{du_i}{dt} = \frac{4\sigma_{\text{SB}} (T_{\text{BGR}}^4 - T_i^4)}{\bar{\Sigma}_i^2 \bar{\kappa}_{\text{R}}(\rho_i, T_i) + \kappa_{\text{P}}^{-1}(\rho_i, T_i)}, \quad (2)$$

where σ_{SB} is the Stefan–Boltzmann constant, T_{BGR} is the pseudo-background temperature below which particles cannot cool radiatively, $\bar{\Sigma}_i$ is mass-weighted mean column density of the particle, and $\bar{\kappa}_{\text{R}}$ and κ_{P} are the Rosseland- and Planck-mean opacities, respectively.

Once most of the gas in the disc has dissipated (accreted on to the central star and on to the secondary objects formed in the disc; $t = 10$ kyr), we utilize an N -body integrator with a fourth-order Hermite integration scheme (Makino & Aarseth 1992), to follow the evolution of the objects present at the end of each hydrodynamic simulation up to 200 kyr. We use a strict timestep criterion so that energy is conserved to better than one part in 10^8 (Hubber & Whitworth 2005). This allows us to determine the ultimate fate of these objects: will they remain bound to central star or be ejected from the system? It is noted that at this phase, we ignore gravitational and dissipative interactions due to gas within the disc.

2.1 Radiative feedback from sinks

Sinks that represent stars, brown dwarfs and planets in the simulations interact both gravitationally and radiatively with the disc. In the optically thin limit, the temperature that the dust/gas will attain at a distance $|\mathbf{r} - \mathbf{r}_n|$ from a radiative object n is

$$T_n(\mathbf{r}) = \left(\frac{L_n}{16\pi\sigma_{\text{SB}}} \right)^{1/4} (|\mathbf{r} - \mathbf{r}_n|)^{-1/2}. \quad (3)$$

In the optically thick limit, considering a geometrically thin, passive disc (e.g. Kenyon & Hartmann 1987) the temperature is

$$T_n(\mathbf{r}) = \left(\frac{L_n R_n}{4\pi\sigma_{\text{SB}}} \right)^{1/4} (|\mathbf{r} - \mathbf{r}_n|)^{-3/4}. \quad (4)$$

Therefore, the temperature drops faster with the distance from the radiative object in the optically thick case ($q = 3/4$ versus $q = 1/2$, respectively). However, in the case of a flared disc the temperature drop is less steep, approaching the $q = 1/2$ value. This is because a flared disc intercepts a higher fraction of the star's radiation (e.g. Kenyon & Hartmann 1987; Chiang & Goldreich 1997). This lower value for q is also consistent with disc observations (e.g. Andrews et al. 2009).

Customarily, the optically thin case is used in analytic and computational studies of protostellar disc evolution (e.g. Matzner & Levin 2005; Kratter & Matzner 2006; Stamatellos et al. 2007b; Offner et al. 2009; Stamatellos & Whitworth 2009b; Stamatellos et al. 2011b; Zhu et al. 2012; Lomax et al. 2014; Vorobyov & Basu 2015; Dong et al. 2016; Kratter & Lodato 2016), albeit with a scaled-down stellar luminosity (by a factor of ~ 0.1) so as to match detailed radiative transfer calculations (see Matzner & Levin 2005). In either case, the temperature at a given distance from a radiative source depends on the luminosity of the source. The luminosity of young stellar and substellar objects is mostly due to accretion of material on to their surfaces.

In the simulations presented here, we assume a time-independent contribution from the central star in the optically thick regime, and a time-dependent contribution in the optically thin regime from the secondary objects that form self-consistently in the simulations. We describe each one in detail in the following sections. We note that these contributions only account for disc heating due to radiation released on the surfaces of bound objects; energy release in the disc mid-plane due to accretion is taken into account self-consistently within the hydrodynamic simulation. This approach ignores the case in which the density of the gas within the Hill radius of a secondary object is high, shielding the rest of the disc from the effect of heating. However, such a phase would be short-lived as gas is accreted on to the secondary object.

2.1.1 Radiative feedback from the central star

We assume that the radiative feedback from the central star is constant with time, and independent of the accretion rate on to it. This is done because the central star is part of the initial conditions and does not form self-consistently in the simulations. Therefore, the accretion rate on to it may not be properly determined. Additionally, by choosing a relatively steep temperature profile, we minimize the role of the central star in stabilizing the disc, and focus on the radiative effect from the secondary objects forming in the disc.

The pseudo-background temperature due to the central star is set to

$$T_{\text{BGR}}^*(R) = \left[T_0^2 \left(\frac{R^2 + R_0^2}{\text{au}^2} \right)^{-3/4} + T_\infty^2 \right]^{1/2}. \quad (5)$$

R is the distance from the star on the disc mid-plane, $R_0 = 0.25$ au is a smoothing radius which prevents non-physical values when $R \rightarrow 0$, $T_0 = 250$ K is the temperature at a distance of 1 au from the central star and $T_\infty = 10$ K is the temperature at large distances from the star. The above equation is chosen purely on numerical grounds to reproduce the required properties of the temperature profile.

2.1.2 Radiative feedback from secondary objects

The radiative feedback from secondary objects depends on the accretion rate of gas on to them, and it is therefore time-dependent. The pseudo-background temperature due to radiative secondary objects in the disc is set to

$$T_{\text{BGR}}^4(\mathbf{r}) = (10 \text{ K})^4 + \sum_n \left(\frac{L_n}{16\pi\sigma_{\text{SB}} |\mathbf{r} - \mathbf{r}_n|^2} \right), \quad (6)$$

where L_n and \mathbf{r}_n are the luminosity and position of a radiative object n (Stamatellos et al. 2011b; Stamatellos et al. 2012; Stamatellos 2015). The luminosity of a radiative secondary object n is set to

$$L_n = L_{\text{NB}} + \frac{f G M_n \dot{M}_n}{R_{\text{acc}}}. \quad (7)$$

The first term on the right-hand side of the equation describes the luminosity of the object from nuclear burning which is set equal to $(M_n/M_\odot)^3 L_\odot$ for stellar objects ($M > 0.08 M_\odot$) and 0 for substellar objects. The second term represents the accretion luminosity. We let $f = 0.75$ be the fraction of accretion energy that is radiated away at the photosphere of the object (Offner et al. 2010). R_{acc} is the accretion radius, set to $R_{\text{acc}} = 3 R_\odot$ (Palla & Stahler 1993). The choice of the accretion radius does not qualitatively affect the results presented in this paper.

We consider three cases of radiative feedback from secondary objects forming in the disc by fragmentation: (i) NRF, (ii) CRF and (iii) ERF. In the case of NRF, objects accrete gas but the accretion energy deposited on their surfaces is not fed back into the disc. In the CRF case, gas accretes on to the object releasing energy that is fed back into the disc through the pseudo-background temperature set by Equations (6)–(7). In the ERF case, mass accretes in periodic bursts resulting in episodic energy release.

The episodic accretion model that we use is described in detail in Stamatellos et al. (2011b) and Stamatellos et al. (2012). Gravitational instabilities cannot develop within the inner regions of a disc (\sim a few au) around a secondary object due to high temperatures. Therefore, there is no mechanism to transport angular momentum outwards for the gas to accrete on to the object, and mass accumulates in the inner disc region. The accumulation of gas increases the density and temperature. When the temperature is sufficiently high to ionize the gas, the MRI is activated, and gas starts flowing on to the secondary object. As with gravitational instability, angular momentum is transported outwards and matter flows inwards. When the mass in the inner accretion disc (IAD) is depleted, the MRI ceases, and mass once again begins to accumulate within the inner disc region.

As the hydrodynamic simulations do not have the resolution to capture the details of the IAD around each secondary object, Stamatellos et al. (2011b) developed a subgrid model to capture the effect of MRI, utilizing the time-dependent episodic accretion model ascribed to Zhu et al. (2010). Each secondary sink is notionally split into two components, the *object* and the IAD such that

$$M_{\text{sink}} = M_{\star} + M_{\text{IAD}}, \quad (8)$$

where M_{\star} is the mass of the object and M_{IAD} is the mass of its IAD. The accretion rate on to the object, \dot{M}_{\star} , is assumed to have two components: a small continuous accretion \dot{M}_{CON} , and the accretion due to the MRI, \dot{M}_{MRI} . The total accretion rate is therefore

$$\dot{M}_{\star} = \dot{M}_{\text{CON}} + \dot{M}_{\text{MRI}}. \quad (9)$$

The material only couples to the magnetic field when it becomes ionized. The temperature at which this occurs is set to $T_{\text{MRI}} \sim 1400$ K. Zhu et al. (2010) estimate that the accretion rate during an episode and the duration of an episode are

$$\dot{M}_{\text{MRI}} \sim 5 \times 10^{-4} \text{ M}_{\odot} \text{ yr}^{-1} \left(\frac{\alpha_{\text{MRI}}}{0.1} \right), \quad (10)$$

and

$$\Delta t_{\text{MRI}} \sim 0.25 \text{ kyr} \left(\frac{\alpha_{\text{MRI}}}{0.1} \right)^{-1} \left(\frac{M_{\star}}{0.2 \text{ M}_{\odot}} \right)^{2/3} \times \left(\frac{\dot{M}_{\text{IAD}}}{10^{-5} \text{ M}_{\odot} \text{ yr}^{-1}} \right)^{1/9}, \quad (11)$$

respectively. \dot{M}_{IAD} is the mass accretion rate which flows on to the IAD, i.e. the accretion rate on to the sink. α_{MRI} is the MRI viscosity α -prescription parameter (Shakura & Sunyaev 1973). The MRI is assumed to occur when sufficient mass has been accumulated within the IAD such that

$$M_{\text{IAD}} > M_{\text{MRI}} \sim \dot{M}_{\text{MRI}} \Delta t_{\text{MRI}}. \quad (12)$$

Substituting in Equations (10) and (11) yields

$$M_{\text{IAD}} > 0.13 \text{ M}_{\odot} \left(\frac{M_{\star}}{0.2 \text{ M}_{\odot}} \right)^{2/3} \left(\frac{\dot{M}_{\text{IAD}}}{10^{-5} \text{ M}_{\odot} \text{ yr}^{-1}} \right)^{1/9}. \quad (13)$$

Observations of FU Orionis stars (see e.g. Hartmann & Kenyon 1996) show that the accretion rate during an outburst episode drops exponentially. We therefore set for the accretion rate on to the central object

$$\dot{M}_{\text{MRI}} = 1.58 \frac{M_{\text{MRI}}}{\Delta t_{\text{MRI}}} \exp \left\{ -\frac{t - t_0}{\Delta t_{\text{MRI}}} \right\}, \quad t_0 < t < t_0 + \Delta t_{\text{MRI}}, \quad (14)$$

t_0 and $t_0 + \Delta t_{\text{MRI}}$ are the temporal bounds of the accretion episode. The factor of $1.58 = e/(e - 1)$ is included to allow all of the mass in the IAD to be accreted on to the object within Δt_{MRI} . The accumulation of mass into the IAD occurs on a time-scale

$$\Delta t_{\text{ACC}} \sim \frac{\dot{M}_{\text{MRI}}}{\dot{M}_{\text{IAD}}}. \quad (15)$$

Using Equation (13) gives

$$\Delta t_{\text{ACC}} \simeq 13 \text{ kyr} \left(\frac{M_{\star}}{0.2 \text{ M}_{\odot}} \right)^{2/3} \left(\frac{\dot{M}_{\text{IAD}}}{10^{-5} \text{ M}_{\odot} \text{ yr}^{-1}} \right)^{-8/9}. \quad (16)$$

Comparing this with Equation (11) shows that the period when mass is being accumulated into the IAD is much longer than the accretion episodes.

The free variables in this model are \dot{M}_{CON} and α_{MRI} . Increasing α_{MRI} yields shorter but more intense accretion episodes. Note that Equations (13) and (16) are independent of α_{MRI} . The uncertainty on α_{MRI} , which lies in the range 0.01–0.4 (King, Pringle & Livio 2007), is therefore not reflected in the mass accreted in an episode nor the time interval between successive episodes.

3 INITIAL CONDITIONS

We study the evolution of a 0.3-M_{\odot} gravitationally unstable protostellar disc around a 0.7-M_{\odot} star. The surface density and temperature profiles of the disc are set to $\Sigma \propto R^{-p}$ and $T \propto R^{-q}$, respectively. The surface density power index p is thought to lie between 1 and 3/2 from semi-analytical studies of cloud collapse and disc creation (Lin & Pringle 1990; Tsukamoto et al. 2015). The temperature power index q has been observed to lie in the range from 0.35 to 0.8 from studies of pre-main sequence stars (Andrews et al. 2009). Here, we adopt $p = 1$ and a relatively high value of $q = 0.75$, in order to minimize the role of the central star in stabilizing the disc and focus on the radiative effect from the secondary objects forming in the disc.

The disc extends from an inner radius $R_{\text{in}} = 1$ au to an outer radius $R_{\text{out}} = 100$ au. The surface density profile we use is

$$\Sigma(R) = \Sigma_0 \left(\frac{R_0^2}{R_0^2 + R^2} \right)^{1/2}, \quad (17)$$

where $\Sigma_0 = 1.7 \times 10^4 \text{ g cm}^{-2}$ is the surface density at $R = 0$. The initial disc temperature profile is set using Equation (5), i.e. initially $T(R) = T_{\text{BG}}^*(R)$. We use $N = 10^6$ SPH particles to represent the disc. These are distributed using random numbers between R_{in} and R_{out} so as to reproduce the disc density profile. The values we use for all the aforementioned parameters are listed in Table 1.

The disc is initially massive enough that it is gravitationally unstable ($Q < 1$) beyond ~ 30 au (see Fig. 1). We have chosen such a profile to ensure that the disc will fragment, so as to study the effect of radiative feedback from secondary objects on subsequent fragmentation. The initial Toomre parameter reaches very low values at the outer edge of the disc which is unrealistic. When a disc forms around a young protostar its mass increases by infalling material from the protostellar envelope. That progressively reduces Q

Table 1. The initial disc parameters. The disc is gravitationally unstable, as determined by the Toomre criterion.

Disc parameter	Value
N	10^6
M_{disc}	$0.3 M_{\odot}$
M_{\star}	$0.7 M_{\odot}$
R_{in}	1 au
R_{out}	100 au
R_0	0.25 au
T_0	250 K
T_{∞}	10 K
p	1
q	0.75

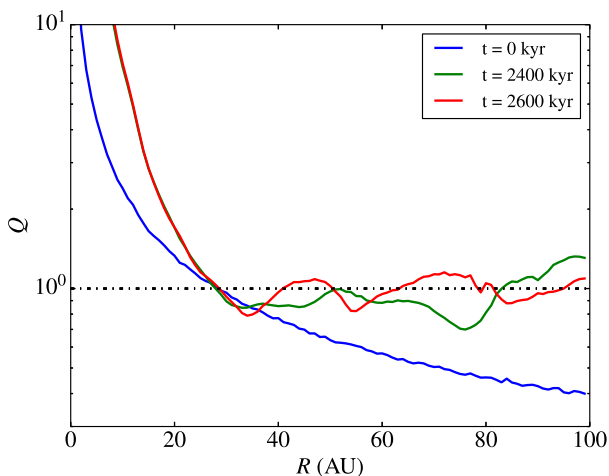


Figure 1. Azimuthally averaged Toomre parameter Q for a disc with the initial conditions listed in Table 1, and at later times (as marked on the graph), before the disc fragments.

to just below ~ 1 and the disc may then fragment (e.g. Stamatellos et al. 2011b). In the simulations that we present here, the initial low Q value results in high effective viscosity, so that the disc attains a nearly uniform $Q \sim 1$ (see Fig. 1, red & green lines) within a few outer orbital periods. This is similar to what it would be expected for a disc forming in a collapsing cloud.

We compute the gravitational acceleration for every disc particle using a spatial octal-tree (Barnes & Hut 1986). The velocity of a particle i in the x - y plane is set using $v_{xy,i} = \sqrt{R_i |g_{xy,i}|}$, where R_i and $g_{xy,i}$ are the radius and the gravitational acceleration of the particle on the disc mid-plane, respectively. We assume that there are no initial motions perpendicular to the disc mid-plane.

The number of SPH particles used to represent the disc (10^6) ensures that gravitational fragmentation can be properly resolved. The minimum resolvable mass for a $0.3 M_{\odot}$ disc comprising 10^6 particles is $3.14 \times 10^{-4} M_{\odot}$. Bate & Burkert (1997) argue that the Jeans mass must be resolved by $2 \times N_{\text{neigh}}$ and Nelson (2006) concludes that the Toomre mass must be resolved by $6 \times N_{\text{neigh}}$. The simulations performed by Stamatellos & Whitworth (2009b) with a $0.7 M_{\odot}$ disc and 1.5×10^5 particles find a minimum Jeans mass of $\sim 2 M_{\odot}$ and a minimum Toomre mass of $\sim 2.5 M_{\odot}$. If we take $2 M_{\odot}$ as a lower resolution limit, then this corresponds to $\sim 128 \times N_{\text{neigh}}$ i.e. the disc is sufficiently resolved. The vertical structure of our disc

is also adequately resolved, since we use ~ 7 times more particles than the simulations of Stamatellos & Whitworth (2009b) where the disc scaleheight is resolved by a factor of more than 3–5 smoothing lengths.

4 DISC FRAGMENTATION AND THE EFFECT OF RADIATIVE FEEDBACK

We perform a set of five simulations of a $0.3 M_{\odot}$ gravitationally unstable protostellar disc around a $0.7 M_{\odot}$ star. The disc initial conditions are identical (as described in Section 3). The disc is gravitationally unstable, thus spiral arms form and the disc fragments to form secondary objects in all five cases (see Table 2). The only difference between the five simulations is the way the radiative feedback from these secondary objects is treated: (i) for simulation ‘NRF’ there is NRF from secondary objects, (ii) for simulation ‘CRF’, the radiative feedback from secondary objects is continuous and (iii) for simulations ‘ERF001’, ‘ERF01’, ‘ERF03’ the radiative feedback is episodic. The difference between the last three simulations is the value of the viscosity parameter due to the MRI, which determines the intensity and the duration of the outburst (ERF001: $\alpha_{\text{MRI}} = 0.01$; ERF01: $\alpha_{\text{MRI}} = 0.1$; ERF03: $\alpha_{\text{MRI}} = 0.3$). The disc surface density and the disc mid-plane temperature of the five runs are shown in Figs 2–6. In all five simulations, the discs evolve identically and at 2.7 kyr an object forms due to gravitational fragmentation. From this point on, the simulations differ as this object provides different radiative feedback in each run. In the NRF run, seven secondary objects form by disc fragmentation, whereas in the CRF run, only one secondary object forms. In the ERF runs, three to four secondary objects form, i.e. somewhere in between the two previous cases, similarly to what previous studies have found (Stamatellos et al. 2011b; Stamatellos et al. 2012; Lomax et al. 2014, 2015). The properties of the objects formed in each run are listed in Table 2. In the next subsections, we discuss each of the simulations in detail.

4.1 No radiative feedback

Fig. 2 shows the evolution of the surface density and mid-plane temperature for the disc whereby NRF is provided from secondary objects that form in the disc. Spiral arms develop and the disc fragments to form seven secondary objects (see Table 2). Fragmentation occurs outside 65 au where the disc is gravitationally unstable and cools fast enough (e.g. Rice et al. 2003a, 2005; Stamatellos et al. 2007a, 2011a). After 10 kyr, the first of these objects has accreted a sufficient amount of gas to become a low-mass hydrogen-burning star ($M = 97 M_{\odot}$). Two brown dwarfs are formed (with masses 48 and $66 M_{\odot}$) and orbit within 25 au of the central star (at 25 and 15 au, respectively). Three of the objects formed remain in the planetary-mass regime. These form at a late stage and at large orbital radii, thus having less time to accrete gas from the disc. One of these planets undergoes a net radial outward migration of 300 au between its formation at 5.9 kyr and the end of the hydrodynamical simulation (10 kyr). These objects are bound to the central star by the end of the hydrodynamic simulation. However, a few of them are loosely bound at large radii ($R > 150$ au for three of them), and therefore destined to be ejected from the system. Indeed, at the end of the NBODY calculation (at 200 kyr), all but two of these objects are ejected from the system, becoming free-floating planets and brown dwarfs (see also Stamatellos & Whitworth 2009a; Li et al. 2015, 2016; Vorobyov 2016).

Table 2. The properties of objects formed by gravitational fragmentation in the simulations with NRF from secondary objects (NRF), with CRF, and with ERF (ERF001, ERF01, ERF03). N_o is the total number of secondary objects formed, t_i is the formation time of an object, M_i its initial mass and M_f its final masses (i.e. at the end of the hydrodynamical simulation; $t = 10$ kyr). M_{MAX} is the maximum possible mass it can attain by accreting mass from the disc (see the discussion in the text). $\langle \dot{M} \rangle$ is the mean accretion rate, \dot{M}_f is the accretion rate on to the object at 10 kyr, R_i is the distance from the star when it forms, R_f is its final distance from the star, and $\Delta R = R_f - R_i$ is its radial migration within 10 kyr. S denotes the central star, LMS secondary low-mass stars, BD brown dwarfs and P planets. In the final column, we mark the boundedness at the end of the NBODY simulation (200 kyr). B and E denote bound and ejected, respectively.

Run ID	α_{MRI}	N_o	t_i (kyr)	M_i (M_J)	M_f (M_J)	M_{MAX} (M_J)	$\langle \dot{M} \rangle$ ($10^{-7} M_{\odot} \text{yr}^{-1}$)	\dot{M}_f ($10^{-7} M_{\odot} \text{yr}^{-1}$)	R_i (au)	R_f (au)	ΔR (au)	Type	Bound
NRF	–	7	0.0	733	773	774	37.7	5.29	0	0	0	S	–
			2.7	2	97	99	124	14.7	77	105	28	LMS	B
			4.3	4	48	53	75.0	27.3	65	25	-40	BD	E
			5.5	2	13	13	22.0	2.83	160	144	-16	P/BD	E
			5.9	2	4	4	4.63	0.02	270	570	300	P	E
			6.0	2	66	67	154	4.57	103	15	-88	BD	B
			7.1	1	4	4	7.78	3.19	191	169	-22	P	E
			7.5	1	3	3	6.33	0.34	103	235	132	P	E
CRF	–	1	0.0	733	772	826	36.8	31.9	0	0	0	S	–
			2.7	2	79	191	100	66.6	77	68	-9	BD/LMS	B
			0.0	733	772	811	37.2	33.0	0	0	0	S	–
			2.7	2	87	127	111	35.0	77	76	-1	LMS	B
ERF001	0.01	4	5.4	3	32	42	60.5	8.54	93	178	85	BD	B
			8.2	2	8	32	31.0	20.7	166	97	-69	P	E
			9.8	2	3	5	51.0	2.01	119	104	-15	P	E
			0.0	733	771	805	37.3	25.2	0	0	0	S	–
ERF01	0.1	3	2.7	2	91	124	117	24.3	77	64	-13	LMS	B
			6.3	3	13	63	26.9	36.4	85	123	38	P/BD	E
			7.9	2	9	25	31.4	11.9	137	129	-8	P	E
			0.0	733	771	782	44.3	33.6	0	0	0	S	–
ERF03	0.3	4	2.7	2	105	116	135	31.2	77	40	-37	LMS	B
			5.5	2	66	73	138	18.5	106	14	-92	BD	B
			6.0	2	17	24	34.9	29.5	87	142	55	BD	E
			6.0	3	16	16	72.0	0.0	96	300	204	BD	E

4.2 Continuous radiative feedback

Fig. 3 shows the evolution of the disc surface density and disc mid-plane temperature for the simulation with CRF from secondary objects that form in the disc. The disc fragments but only one secondary object forms. CRF from this object heats and stabilizes the disc; therefore, no further fragmentation occurs. The object carves out a gap within the disc and migrates inwards 9 au by the end of the hydrodynamical simulation (i.e. within 7.3 kyr since its formation). At this point, it has accreted enough gas to become a high-mass brown dwarf and is close to overcoming the hydrogen-burning mass limit. As there is still plenty of gas within the disc, the ultimate fate of this system is a binary comprising a solar-type and a low-mass secondary star.

4.3 Episodic radiative feedback

Figs 4–6 show the surface density and disc mid-plane temperature evolution for the simulations with ERF from secondary objects forming in the disc, in three different cases: $\alpha_{\text{MRI}} = 0.01, 0.1, 0.3$, respectively. The disc fragments as in the previous cases; the radiative feedback from secondary objects is now episodic due to episodic accretion. During the accretion/outburst episodes, the mass that has accumulated in the inner disc region of a secondary object flows on to the object, resulting in an increase of its accretion luminosity that affects a large portion of the disc around the central star. This is evident by the sudden increase in the temperature (e.g. in Figs 4

and 5). The increase of the temperature in the disc is three- to four-fold (see Fig. 7b), which is enough to stabilize the disc during the outburst. However, in all three cases, when the outburst stops, the disc becomes unstable and fragments.

The number of secondary objects formed is similar in all three cases (three to four objects). Therefore, fewer objects form than in the non-radiative feedback case and more objects than the CRF case (Stamatellos et al. 2011b; Stamatellos et al. 2012; Lomax et al. 2014, 2015).

The frequency and duration (see Table 3) of the accretion/feedback outbursts are important for the gravitational stability of the disc. The total duration of episodic outbursts drops from ~ 18 to ~ 0.8 per cent of the simulated disc lifetime (10 kyr), as the viscosity parameter α_{MRI} is increased from 0.01 to 0.3. A larger α_{MRI} results in stronger but shorter outbursts. The number of secondary objects forming in the disc does not strongly depend on α_{MRI} , which indicates that for suppressing disc fragmentation the total duration of episodic outbursts must be longer.

We find that the average mass of secondary objects at the end of the hydrodynamical simulation (10 kyr) increases with α_{MRI} ; the average masses are 33, 38 and 51 M_J for $\alpha_{\text{MRI}} = 0.01, 0.1$ and 0.3, respectively. In all cases, the two lowest mass objects are ultimately ejected from the system. For $\alpha_{\text{MRI}} = 0.01$, the two lowest mass objects are planets. For $\alpha_{\text{MRI}} = 0.1$, the two lowest mass objects consist of a planet and a brown dwarf. And finally, for $\alpha_{\text{MRI}} = 0.3$, the two lowest mass objects are brown dwarfs. The estimated maximum mass that all of these objects will eventually attain (see next

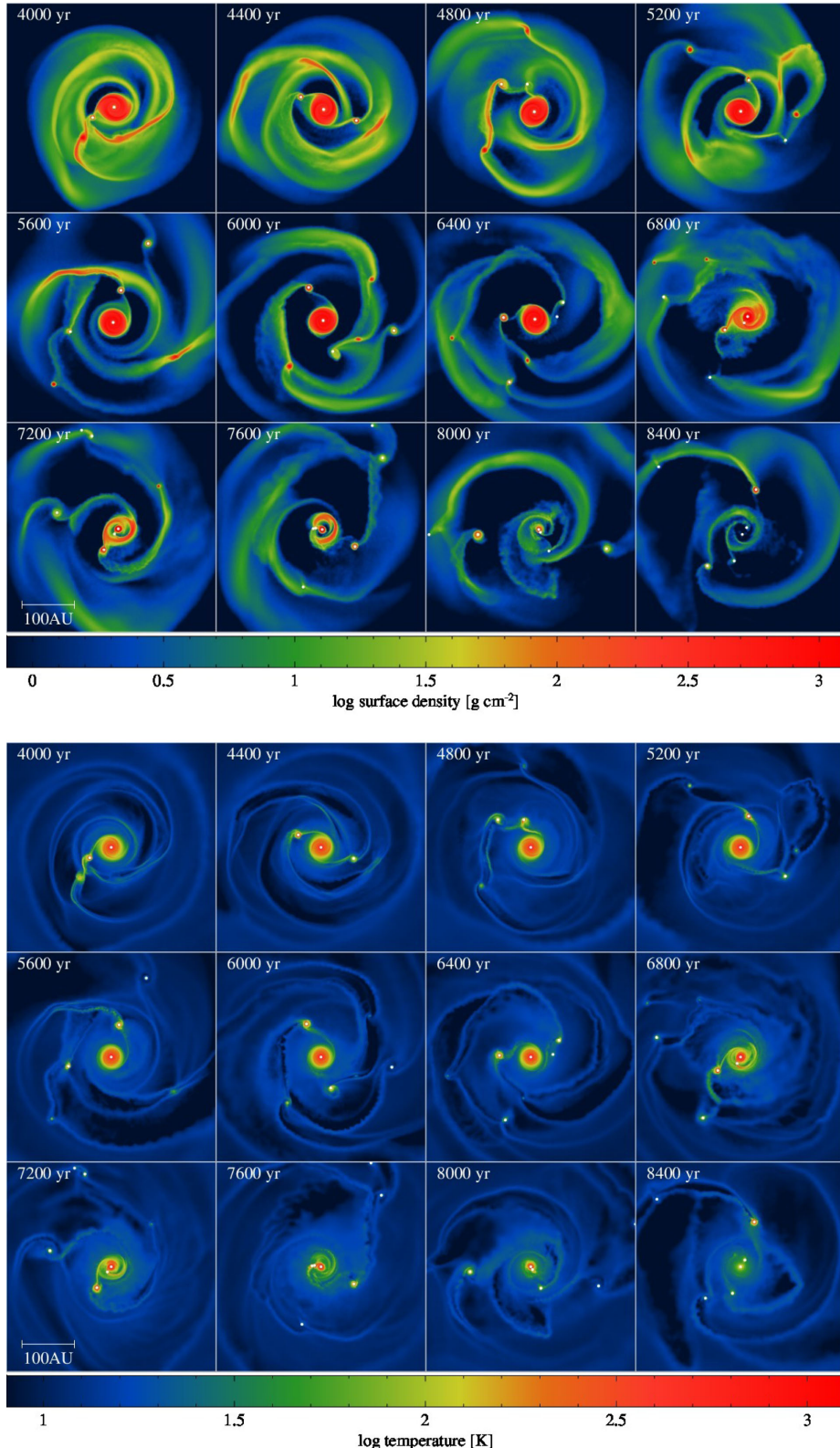


Figure 2. Disc evolution without any radiative feedback from secondary objects (NRF run). The top snapshots show the disc surface density and the bottom snapshots show the disc mid-plane temperature (at times as marked on each graph). Seven objects form by gravitational fragmentation due to the disc cooling fast enough in its outer regions. Most of the objects formed are brown dwarfs and planets. Planets are ultimately ejected from the system.

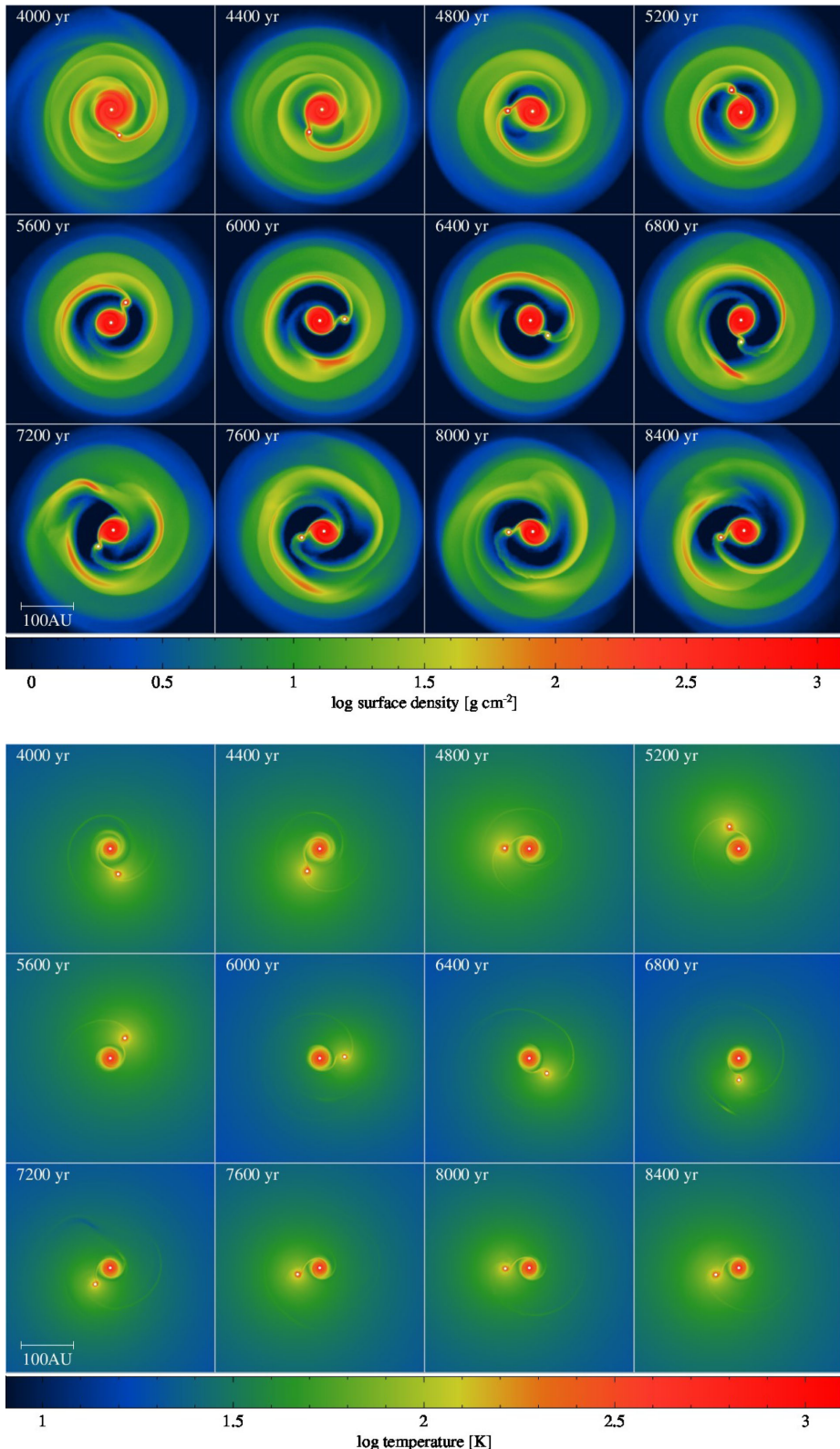


Figure 3. Disc evolution with CRF from secondary objects (CRF run). The disc fragments but only one object forms that ends up as a low-mass star. Radiative feedback from this object suppresses further fragmentation. The object forms on a wide orbit (68 au) and migrates inwards only by 9 au within 7.3 kyr.

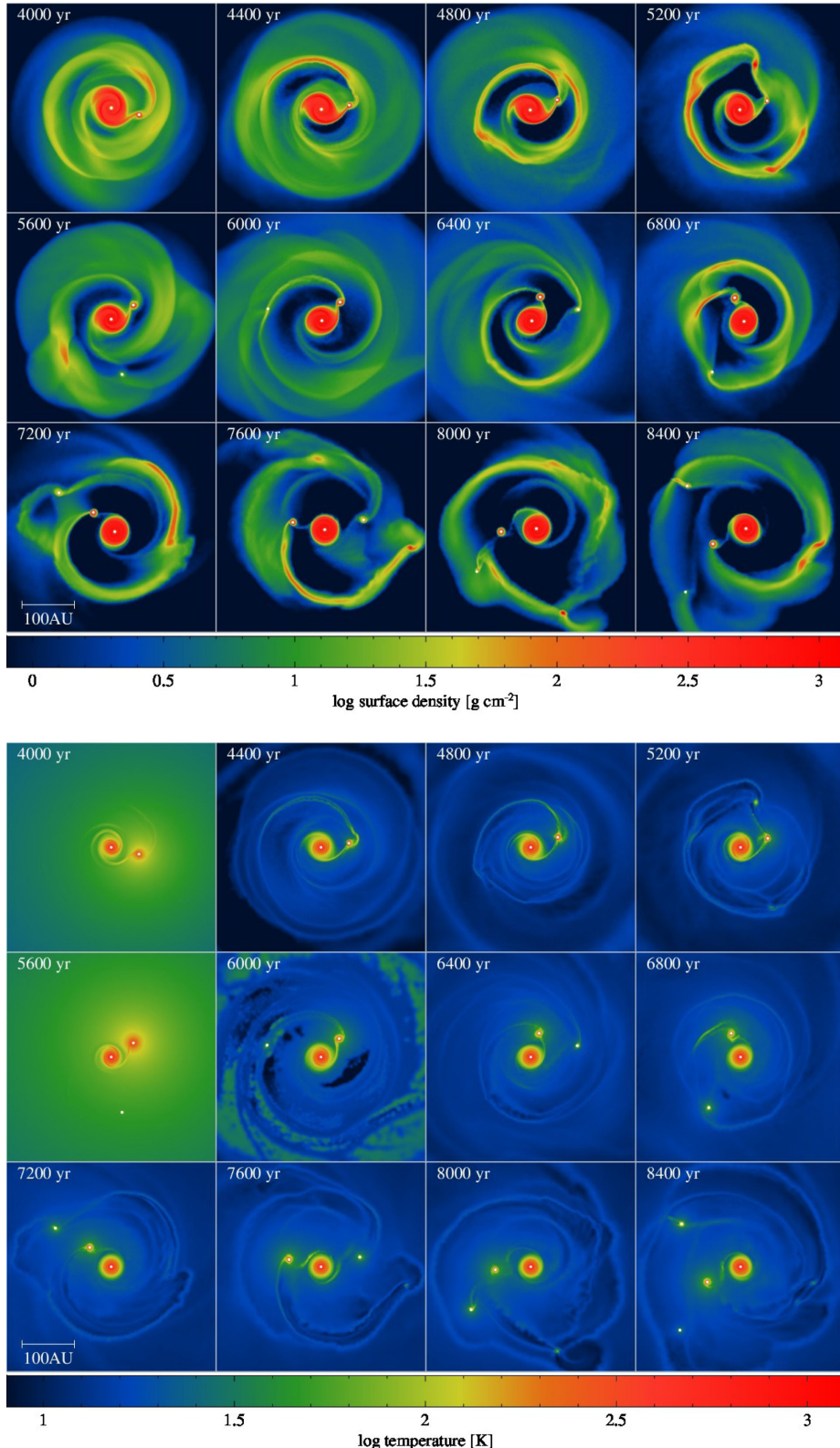


Figure 4. Disc evolution with ERF from secondary objects and a viscosity parameter $\alpha_{\text{MRI}} = 0.01$ (ERF001 run). The disc fragments and four objects form as the disc is cool enough to be gravitationally unstable between accretion episodes.

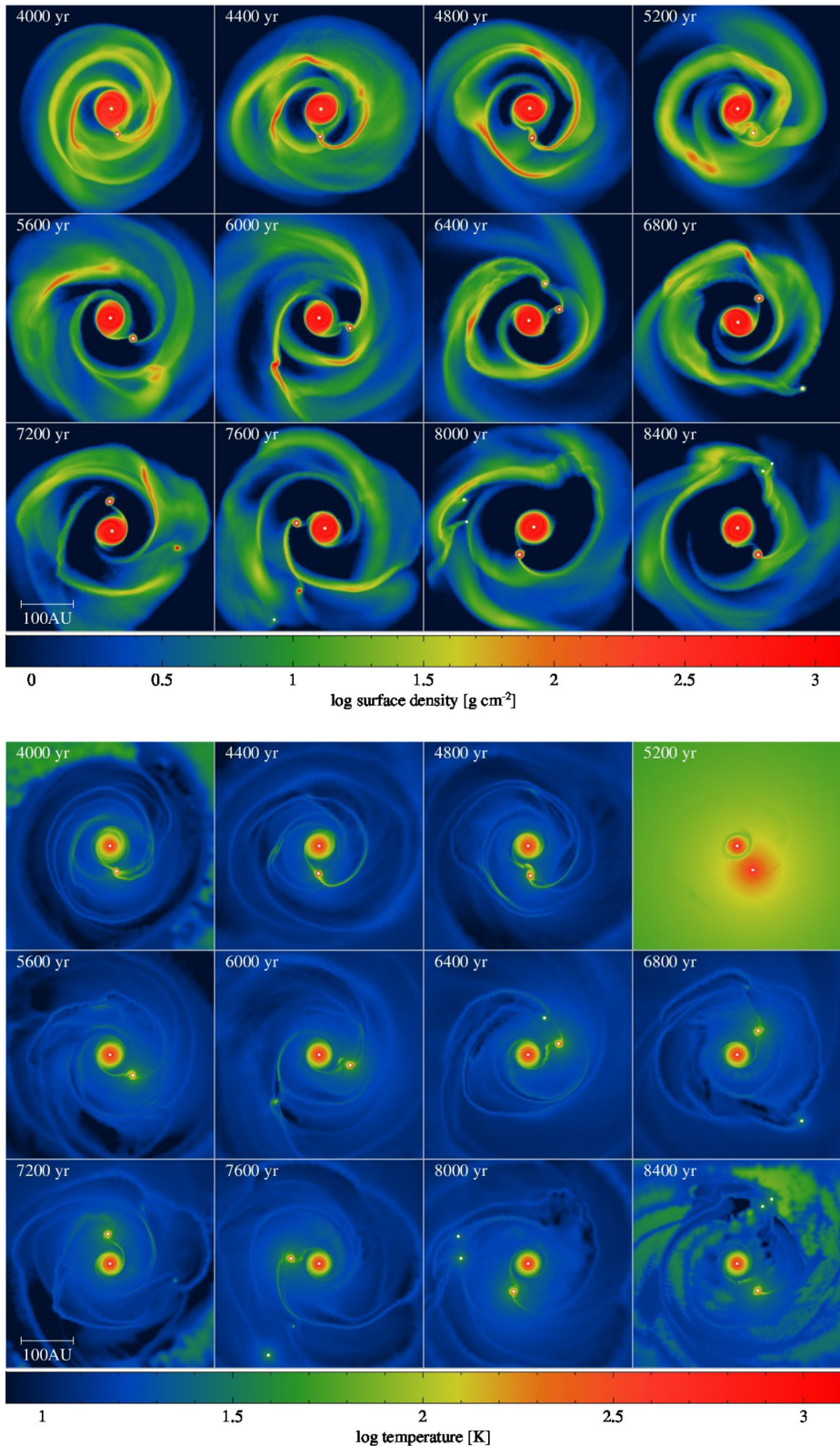


Figure 5. Disc evolution with ERF from secondary objects and a viscosity parameter $\alpha_{\text{MRI}} = 0.1$ (ERF01 run). The disc fragments and three objects form. Two of these objects are planets, as in the ERF001 run.

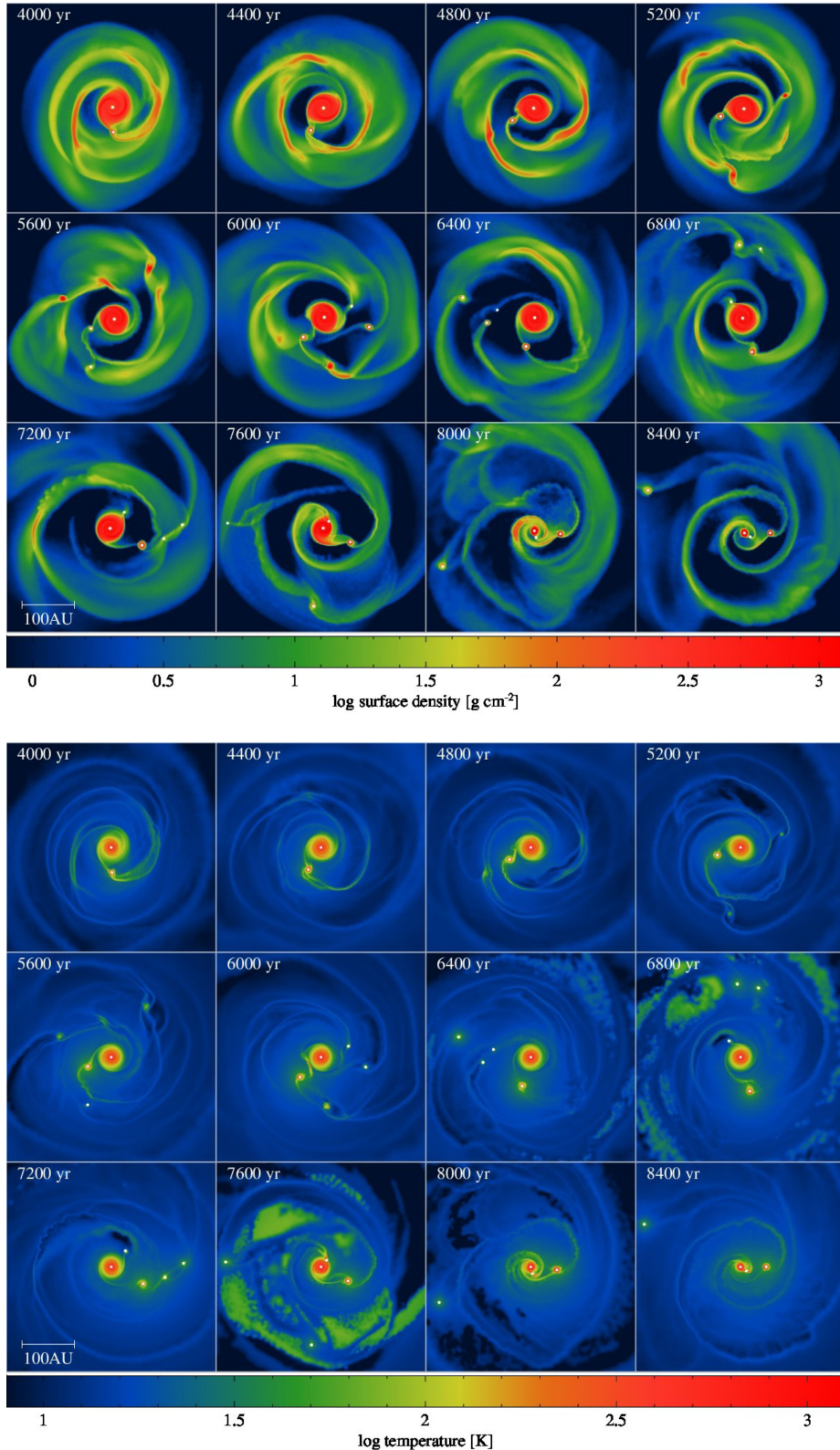


Figure 6. Disc evolution with ERF from secondary objects and a viscosity parameter $\alpha_{\text{MRI}} = 0.3$ (ERF03 run). The disc fragments and four objects form. One object migrates significantly such that it accretes a large amount of gas while in a close orbit to the central star. The two lowest mass objects are ultimately ejected from the system.

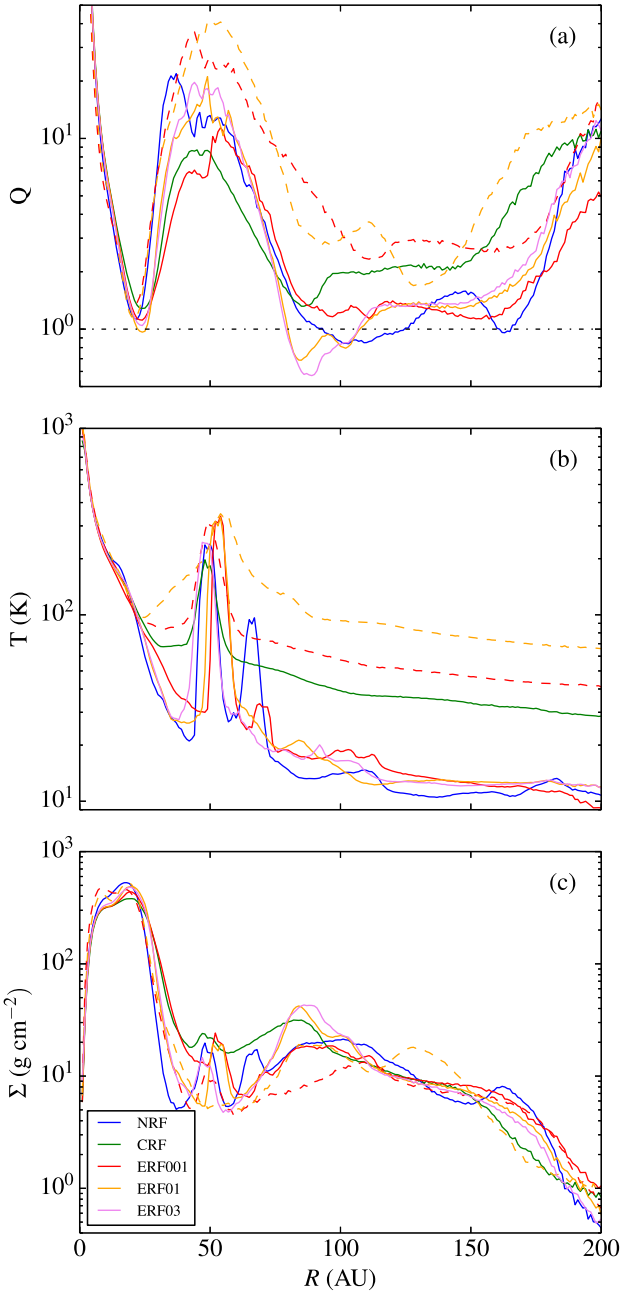


Figure 7. (a) Azimuthally averaged Toomre parameter Q , (b) disc mid-plane temperature, and (c) disc surface density for all simulations at $t = 4.4$ kyr. The coloured dashed lines correspond to times when outburst episodes are happening: $t = 5.6$ kyr and $t = 5.2$ kyr for the simulations ERF001 and ERF01, respectively. The disc inner region is gravitationally stable due to the high temperature, whereas the disc is unstable outside ~ 70 au. The temperature peaks between 50 and 100 au correspond to regions close to secondary objects.

section) is above the deuterium-burning limit, except for one object in the $\alpha_{\text{MRI}} = 0.01$ run.

We further find that subsequent formation of secondary objects happens on a more rapid time-scale for greater values of α_{MRI} . Radiative feedback episodes are shorter for a higher α_{MRI} : the disc cools fast after an episode ends, becoming gravitationally unstable and fragments again within a shorter time.

Table 3. The duration of episodic accretion events from each secondary object in the simulations which consider ERF.

Run ID	α_{MRI}	Sink #	Episodes	Duration (yr)
ERF001	0.01	2	3	1170
		3	2	487
		4	1	90
		5	0	0
		All	6	1747
ERF01	0.1	2	3	108
		3	1	10
		4	1	9
		All	5	128
ERF03	0.3	2	3	46
		3	2	22
		4	1	4
		5	2	9
		All	6	81

4.4 Comparison of simulations with different radiative feedback from secondary objects

Table 2 lists information pertaining to the secondary objects that form in the disc simulations. We list the number of objects formed in each simulation, their initial and final masses (i.e. at the end of the hydrodynamical simulation, $t = 10$ kyr), and an estimate of the maximum mass they can ultimately attain (considering that they will still be evolving in a gaseous disc), the gas accretion rate on to them, their formation and final radius, their type and their estimated boundedness at the end of the NBODY simulation (200 kyr).

The maximum mass, M_{MAX}^i , that an object i can attain is calculated as follows. We assume that each object will continue to accrete at its accretion rate (\dot{M}_f^i) at the end of the hydrodynamic simulation (which is likely an overestimate as generally the accretion rate decreases, unless there is some kind of violent interaction within the disc). Therefore, the maximum mass that an object i can attain is

$$M_{\text{MAX}}^i = M_f^i + \dot{M}_f^i t_{\text{acc}}, \quad (18)$$

where M_f^i is the mass of an object i at $t = 10$ kyr and t_{acc} is the time for which it will keep on accreting gas. We also assume that only a fraction $\xi = 0.9$ of all the gas from the disc could eventually accrete either on to the central star or on to the secondary objects, therefore

$$\xi M_{\text{disc}} = \sum_{\text{sec}} M_f^i + \sum_{\text{all}} \dot{M}_f^i t_{\text{acc}}, \quad (19)$$

where the first sum on the right-hand side is over the secondary objects and the second sum is over all objects to include gas accreting on to the central star. We assume that the accretion time t_{acc} is the same for all objects within each simulation, therefore it is calculated such that

$$t_{\text{acc}} = \frac{\xi M_{\text{disc}} - \sum_{\text{sec}} M_f^i}{\sum_{\text{all}} \dot{M}_f^i}. \quad (20)$$

The maximum estimated mass for an object i can then be calculated using Equation (18).

The number of secondary objects that form in the disc is strongly affected by the type of their radiative feedback. We find that without radiative feedback, seven objects form within the disc (Fig. 2) compared to only one object forming where CRF is considered (Fig. 3). CRF from the secondary object raises the disc temperature

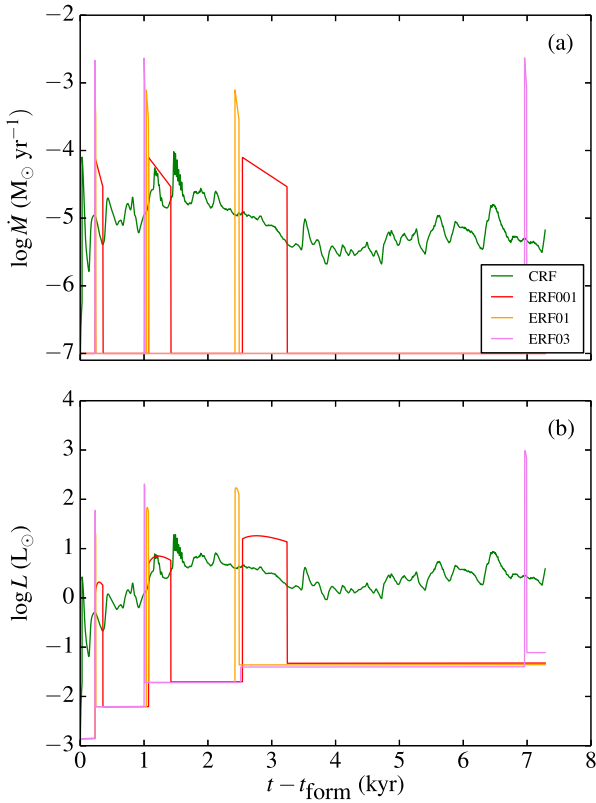


Figure 8. (a) Mass accretion rates onto and (b) accretion luminosities of the first secondary object that forms in each of the simulations where radiative feedback is considered. Time is given with respect to the formation time of each object. At their initial stages of their formation, secondary objects are high accretors and they may even outshine the central star. In the case where radiative feedback is episodic, this only happens for a short time and therefore would be difficult to observe. In the case of CRF (which is probably not realistic), secondary objects may outshine the central star for longer.

enough (see Fig. 7b) to stabilize the disc (Fig. 7a) and suppress further fragmentation. The number of objects when ERF is considered is in between the two previous cases (three to four objects). This behaviour has been seen in previous simulations (Stamatellos et al. 2011b; Stamatellos et al. 2012; Lomax et al. 2014, 2015).

Radiative feedback from secondary objects affects the entire disc as these secondary objects are high accretors (at their initial stages of their formation). For a short time, they may even outshine the central star (see Fig. 8). The assumed pseudo-background temperature profile provided by each secondary object (see Equation 6) influences the temperature at a given location in the disc and may affect disc fragmentation (Stamatellos et al. 2011a) but probably not significantly. If we adopt a pseudo-background temperature profile with $q = 3/4$ instead of $q = 1/2$, then the disc temperature at a distance 50 au from a radiative object will be a factor of ~ 5 smaller, and the Toomre parameter Q (see Fig. 7a) a factor of ~ 2 smaller, bringing it (for the CRF and ERF runs) close to the critical value for fragmentation ($Q \approx 1$; see e.g. Durisen et al. 2007). However, this is the maximum expected effect. Even in the case of $q = 3/4$ (which is an upper limit for q), the disc temperature is expected to be higher than the minimum ‘background’ value due to energy dissipation within the disc as it is gravitationally unstable.

With regard to the ERF runs, the number of secondary objects does not vary much for a different MRI viscosity parameter α_{MRI} . Four objects form when $\alpha_{\text{MRI}} = 0.01$; three objects form when

$\alpha_{\text{MRI}} = 0.1$; and four objects form when $\alpha_{\text{MRI}} = 0.3$. More secondary objects result in more radiative feedback episodes and a hotter disc for longer periods of time. Thus, this provides sustained stability against gravitational fragmentation. The duration of episodic outbursts affects the stability of the disc. For a smaller α_{MRI} , episodes are longer and provide longer periods of stability. The opposite is true for a larger α_{MRI} . This is shown in Table 3. However, it is evident that episodic feedback from only one or two secondary objects cannot suppress further disc fragmentation, in contrast with the continuous feedback case, where the presence of just one secondary object suppresses fragmentation.

Observations of episodic outbursts from secondary objects do not require high-sensitivity; during these outbursts their luminosity increases from a few L_\odot to tens of L_\odot (see Fig. 8). In the case of $\alpha_{\text{MRI}} = 0.01$, where the outburst events are mild and long, 18 per cent of the initial 10 kyr of the disc’s lifetime correspond to the outburst phase. On the other hand, when $\alpha_{\text{MRI}} = 0.3$, where the events are short and intense, this percentage drops down to just 0.8 per cent (see Table 3). However, episodic accretion events are expected to be relatively more frequent only during the initial stages of disc evolution, i.e. within a few kiloyears after the disc’s formation, while the newly formed secondary objects are vigorously accreting gas from the disc. Therefore, such outbursts from secondary objects at the initial stages of disc evolution should not significantly influence the observed number of outbursting sources. Scholz, Froebrich & Wood (2013) observed a sample of ~ 4000 young stellar objects over a period of 5 yr and they found one to four possible outbursting sources indicating that outbursts happen at intervals of (5–50) kyr; this is roughly consistent with our models after the initial ~ 4 kyr during the disc’s evolution (see Fig. 8).

Fig. 7 shows a comparison between radially averaged Toomre parameter, temperature and surface density for a representative snapshot from each simulation exhibiting strong spiral features ($t = 4.4$ kyr). Within the inner ~ 25 au, the disc is stable due to heating from the central star. The peaks in surface density and temperature around ~ 50 au correspond to regions around secondary objects. The discs are unstable or close to being unstable outside ~ 80 au in all cases apart from the CRF run and the ERF runs (during episodic outbursts).

In all simulations, disc fragmentation occurs beyond radii ~ 65 au (see Fig. 9a), where the disc is gravitationally unstable and can cool fast enough (e.g. Stamatellos & Whitworth 2009a). The initial mass of a fragment is a few M_\odot , as set by the opacity limit for fragmentation (Low & Lynden-Bell 1976; Rees 1976). The masses of the secondary objects at the end of the hydrodynamical simulations are shown in Fig. 10. The first object that forms in each simulation generally migrates inwards and accretes enough mass to become a low-mass star; this object remains ultimately bound to the central star. All secondary objects increase in mass as they accrete gas from the disc. However, roughly half of the objects formed in each simulation (excluding CRF) remain as planets by the end of the hydrodynamical simulation as shown in Fig. 10.

In the CRF simulation, the mass growth of the secondary object is mildly suppressed (Figs 11 a and 12a) due to an increased outward thermal pressure, so that the final mass of the object is within the brown dwarf regime. Secondary objects that form at later times tend to have lower masses (Fig. 10).

Episodic feedback also mildly suppresses the mass growth of the first secondary object that forms (Fig. 11a). Its effect is more pronounced for the second secondary object (Fig. 11b). However, the mass growth of each object also depends on where the object forms in the disc and how it interacts both with other objects and with the spiral structure of the disc. Therefore, the mass growth of

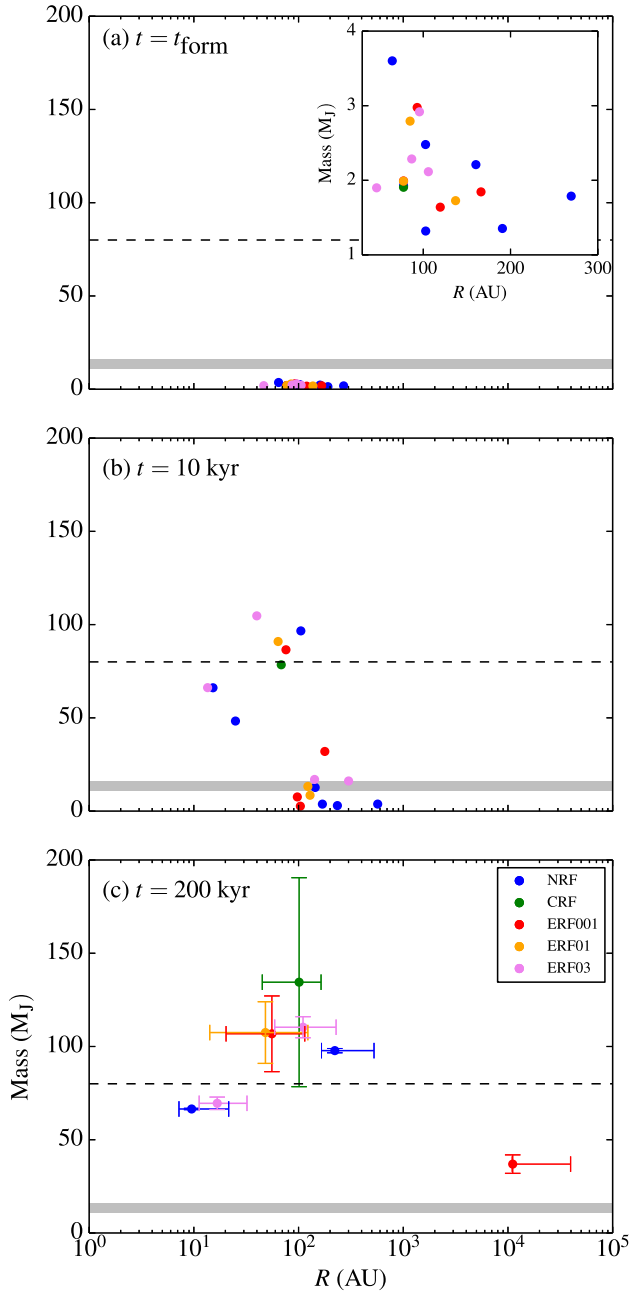


Figure 9. Mass–radius plots of the secondary objects formed by disc fragmentation in all five simulations. (a) Mass and radius at formation. A zoomed inset panel is shown for clarity. (b) Mass and radius at the end of the hydrodynamical simulation (10 kyr). (c) Mass and semimajor axis at the end of the NBODY simulation (200 kyr). The upper mass limits correspond to the maximum mass that the object may attain (see the text for details), whereas the lower mass limits correspond to the mass of the object at the end of the hydrodynamical simulation. The horizontal bars in this panel represent the periastron and apoastron of the secondary object’s orbit around the central star. The dashed line represents the hydrogen burning limit, and the grey band the deuterium burning limit ($\sim 11\text{--}16 M_J$; Spiegel, Burrows & Milsom 2011).

an object can be rather erratic, e.g. for the second object at around 2 kyr (Fig. 11b). Specifically, this object migrates into the high-density region surrounding the central star where it rapidly accretes a large amount of gas (see Fig. 6, 7.2–8 kyr). The effect of episodic

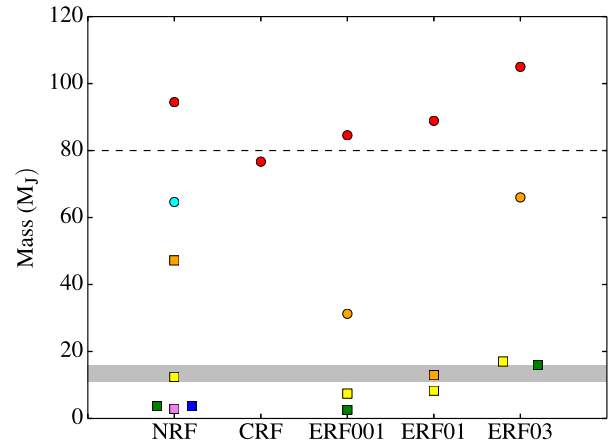


Figure 10. The masses of the secondary objects at the end of the hydrodynamic simulations (10 kyr). Colour denotes the order in which each secondary object formed; from earliest to latest: red, orange, yellow, green, cyan, blue and violet. Circles and squares correspond to objects that are ultimately bound or ejected (at 200 kyr), respectively. The lower points in the NRF and ERF03 simulations are separated for clarity. The dashed line represents the hydrogen burning limit ($\sim 80 M_J$). The grey band represents the deuterium burning limit.

accretion is to suppress mass accretion during/after the outburst (e.g. Fig. 12 a compares NRF and ERF runs after the first outburst; also seen in Figs 12b, c). However, the accretion rate is restored to its previous value within 200–400 yr. Ultimately, there is no strong anticorrelation between the mass that an object and the number and duration of the episodic outbursts it undergoes.

We find a population of planetary-mass objects on wide orbits (100–800 au) around the central star. However, these objects are loosely bound to the central star and could be liberated into the field becoming free-floating planets. We follow the evolution of these systems using NBODY simulations. Indeed, we find that all planetary-mass objects are ejected from the discs (Fig. 10c); what is left behind is a central star with low-mass star or brown dwarf companions. Consequently, it is unlikely that the observed wide-orbit giant planets (Kraus et al. 2008, 2014; Marois et al. 2008; Faherty et al. 2009; Ireland et al. 2011; Kuzuhara et al. 2011, 2013; Aller et al. 2013; Rameau et al. 2013; Bailey et al. 2014; Galicher et al. 2014; Naud et al. 2014; Macintosh et al. 2015) may form by disc fragmentation, unless somehow the mass growth of secondary objects forming in the disc is suppressed. On the other hand, disc fragmentation may readily produce free-floating planets and brown dwarfs (Stamatellos & Whitworth 2009a; Hao, Kouwenhoven & Spurzem 2013; Li et al. 2015; Vorobyov 2016).

Note however that in order to follow the long-term evolution of the system, we have ignored the effect of the gas once the hydrodynamical simulation has evolved for 10 kyr. The effect of gas is to stabilize the system. Therefore, it is possible that some of these planets may remain bound to the central star. However, they should co-exist with a higher mass object (like e.g. a low-mass star or a brown dwarf) and they may accrete enough mass to become brown dwarfs.

4.5 Caveats of sink particles

Sink particles are used in the simulations to prevent large running times. In dense regions, timesteps become very short and without sinks the simulation effectively stalls.

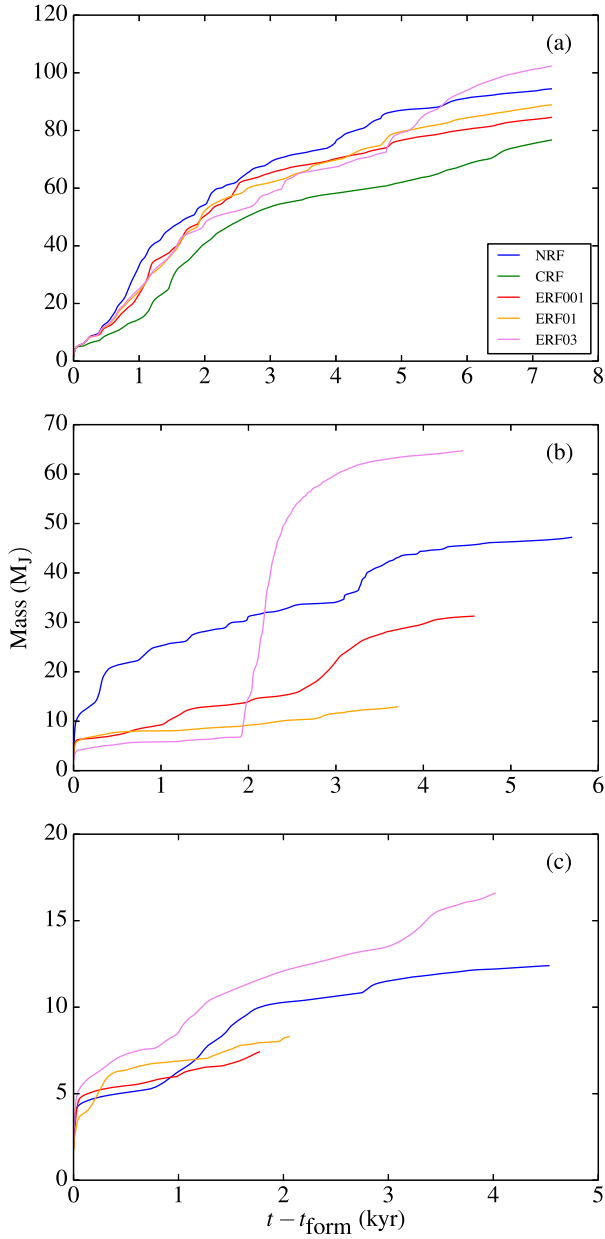


Figure 11. The mass evolution of the first three secondary objects that form in each of the five simulations (for the simulations with ERF the mass refers to the sink mass, i.e. both the object and the IAD). Time is given with respect to the formation time of each object. The second object in the ERF03 run (b) undergoes a rapid increase in mass as it migrates into a dense region around the central star.

In our simulations, a sink particle is created when the density exceeds $10^{-9} \text{ g cm}^{-3}$. It is therefore assumed that if a protofragment reaches this density, it will continue to contract to heat to $\sim 2000 \text{ K}$ such that molecular hydrogen dissociates to initiate the second collapse. The protofragment will ultimately reach stellar densities ($\sim 1 \text{ g cm}^{-3}$) to become a bound object. The density threshold used for sink creation is higher than the density required for the formation of the first hydrostatic core ($\sim 10^{-13} \text{ g cm}^{-3}$). Therefore, the protofragment at this stage contracts on a Kelvin–Helmholtz time-scale. The time that it takes a protofragment to evolve from the first to second hydrostatic core is $\sim 1\text{--}10 \text{ kyr}$ (Stamatellos & Whitworth 2009b). Thus, it is possible that some of the

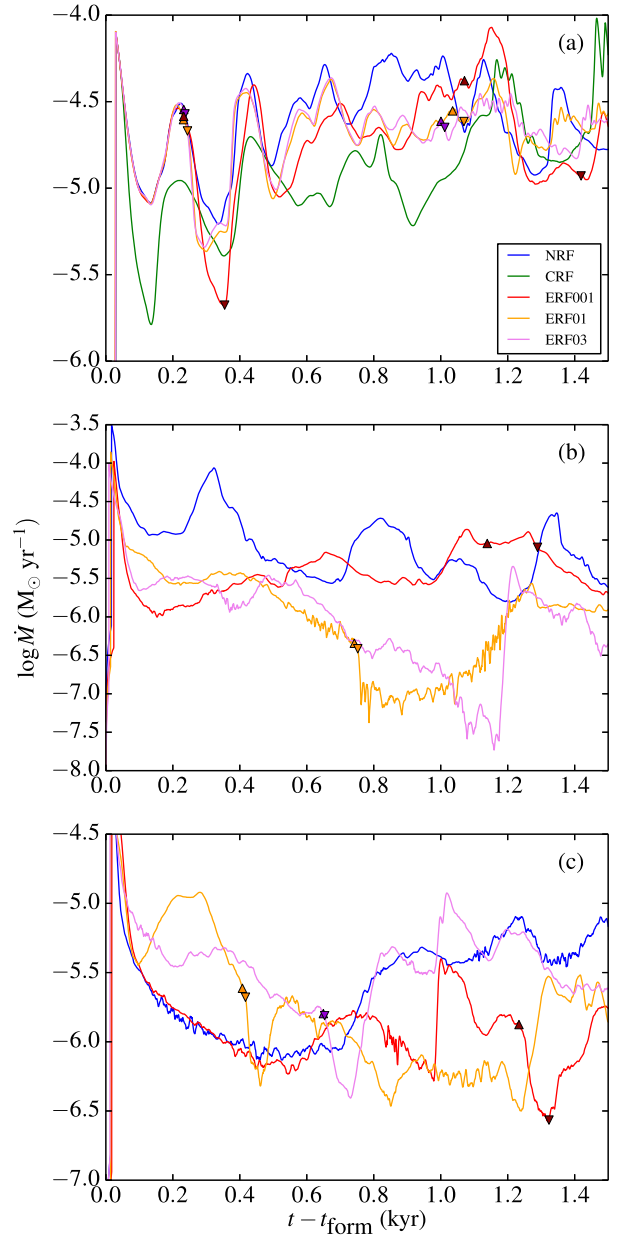


Figure 12. Mass accretion rates on to the first three secondary object that form in each of the five simulations (for the simulations with ERF the accretion rates on to the sinks are plotted). Time is given with respect to the formation time of each object. Upward pointing triangles represent the beginning of accretion episodes in the ERF runs. These are followed by corresponding downward pointing triangles denoting the end of episodes.

protofragments may get disrupted e.g. by interactions with spiral arms and/or tidal forces, and dissolve (Stamatellos & Whitworth 2009b; Zhu et al. 2012; Tsukamoto, Machida & Inutsuka 2013).

Another limitation in the use of sink particles relates to their size. We assume that the sink radius of secondary objects that form in the disc is 1 au, which roughly corresponds to the size of the first hydrostatic core during the collapse of a protofragment (Masunaga & Inutsuka 2000; Tomida et al. 2013; Vaytet et al. 2013). The size of the Hill radius of protofragments that form in the disc is of the order of a few astronomical units. Therefore, a significant fraction of the accretion disc around a protofragment is not resolved. The

flow of material from the sink radius to the secondary object is considered to be instantaneous, whereas, in reality, there is a time delay. This results in increased accretion on to secondary objects, which in the case of continuous feedback results in an increased luminosity. As such, we may overestimate the effect of luminosity on disc fragmentation. However, for the episodic accretion runs we employ a subgrid model (within a sink radius) based on an α -viscosity prescription that allows gas to flow (episodically) on to the secondary object (see Section 2.1.2). Even in this case, the accretion rate is possibly overestimated, as the IAD within the sink (<1 au) does not exchange angular momentum with the rest of the accretion disc (for an additional discussion of this issue, see Hubber, Walch & Whitworth 2013). Nevertheless, considering the uncertainties in α_{MRI} (which in effect modulates the accretion of material on to the secondary objects and for which we examine a wide range of values, all of which lead to similar outcomes), we have confidence that the choice of sink size does not qualitatively affect the results of this paper regarding the effect of radiative feedback on disc fragmentation.

5 CONCLUSIONS

We have performed SPH simulations of gravitationally unstable protostellar discs in order to investigate the effect that radiative feedback from secondary objects formed by fragmentation has on disc evolution. We have considered three cases of radiative feedback from secondary objects: (i) NRF: where no energy from secondary objects is fed back into the disc; (ii) CRF: where energy, produced by accretion of material on to the surface of the object is continuously fed back into the disc; and (iii) ERF: where accretion of gas on to secondary objects is episodic, resulting in ERF. Our findings are summarized as follows.

(i) Radiative feedback from secondary objects that form through gravitational fragmentation stabilizes the disc, reducing the likelihood of subsequent fragmentation. When there is NRF from secondary objects, seven objects form, compared to a single object forming when radiative feedback is continuous. When radiative feedback happens in episodic outbursts, three to four objects form. This is because the disc cools sufficiently to become gravitationally unstable between the outbursts. All objects in the three different radiative feedback cases that we examine here form at radii >65 au, with initial masses of a few M_{\odot} .

(ii) The mass growth of secondary objects is mildly suppressed due to their radiative feedback. The mass of the first object that forms within the disc is generally larger when there is NRF; in the case when radiative feedback is continuous, the mass of the first secondary object is the lowest. ERF tends to reduce the mass accretion rate on to a secondary object during and after an episode outburst. However, the accretion rate is restored to its previous value relatively quickly (within ~ 200 –400 yr).

(iii) The intensity and the duration of an outburst (which in our models is determined by the effective viscosity due to the MRI, α_{MRI}) do not affect the number of objects that form within the disc when ERF is considered. The total duration of the radiative feedback outbursts is not long enough to fully suppress disc fragmentation. However, we find that α_{MRI} affects the average mass of the objects formed: lower α_{MRI} results into lower mass secondary objects. Moreover, subsequent fragmentation happens faster for higher α_{MRI} , as the first outburst finishes faster. The first object that forms in each case undergoes a larger inward migration for increased values of α_{MRI} .

(iv) Regardless of the type of radiative feedback, we find that the first object that forms within the disc, remains ultimately bound to the central star. It accretes mass while it generally migrates inwards. Brown dwarfs also form in the simulations and a fraction of them remain bound to the central star. Gravitational fragmentation may therefore provide a method for the formation of intermediate separation, low-mass-ratio binary systems.

(v) A significant fraction (~ 40 per cent, dropping to ~ 20 per cent if the estimated final mass is considered) of the secondary objects formed by disc fragmentation are planets, regardless of the type of radiative feedback. However, every planet that forms within the disc is ultimately ejected from the system. We do not find any giant planets that remain on wide-orbits around the central star. Secondary objects that form and remain within the disc accrete enough mass to become brown dwarfs, even in the case where radiative feedback suppresses gas accretion. Thus, gravitational fragmentation may produce free-floating planets and brown dwarfs, but not wide-orbit gas giant planets, unless the mass growth of fragments forming in a young protostellar disc is further suppressed.

ACKNOWLEDGEMENTS

We would like to thank the referee A. Boley for his thorough review of the paper. The simulations presented in this paper were performed at UCLan High Performance Computing Facility WILDCAT. Surface density plots were produced using the SPLASH software package (Price 2007). *N*-body simulations were performed by a code originally developed by D. Hubber, who we thank for the support provided. AM is supported by STFC grant ST/N504014/1. DS is partly supported by STFC grant ST/M000877/1.

REFERENCES

- Aller K. M. et al., 2013, ApJ, 773, 63
- Andrews S. M., Wilner D. J., Hughes A. M., Qi C., Dullemond C. P., 2009, ApJ, 700, 1502
- Armitage P. J., Livio M., Pringle J. E., 2001, MNRAS, 324, 705
- Attwood R. E., Goodwin S. P., Stamatellos D., Whitworth A. P., 2009, A&A, 495, 201
- Audard M. et al., 2014, in Beuther H., Klessen R., Dullemond C., Henning T., eds, Protostars and Planets VI. Univ. Arizona Press, Tucson, AZ, p. 387
- Bailey V. et al., 2014, ApJ, 780, L4
- Barnes J., Hut P., 1986, Nature, 324, 446
- Bate M. R., 2009, MNRAS, 392, 1363
- Bate M. R., Burkert A., 1997, MNRAS, 288, 1060
- Bate M. R., Bonnell I. A., Price N. M., 1995, MNRAS, 277, 362
- Bell K. R., Lin D. N. C., 1994, ApJ, 427, 987
- Boley A. C., 2009, ApJ, 695, L53
- Boley A. C., Hayfield T., Mayer L., Durisen R. H., 2010, Icarus, 207, 509
- Bonnell I., Bastien P., 1992, ApJ, 401, L31
- Boss A. P., 1988, ApJ, 331, 370
- Chiang E. I., Goldreich P., 1997, ApJ, 490, 368
- Dong R., Vorobyov E., Pavlyuchenkov Y., Chiang E., Liu H. B., 2016, ApJ, 823, 141
- Dunham M. M., Vorobyov E. I., 2012, ApJ, 747, 52
- Dunham M. M., Evans N. J., Terebey S., Dullemond C. P., Young C. H., 2010, ApJ, 710, 470
- Dupuy T. J., Kratter K. M., Kraus A. L., Isaacson H., Mann A. W., Ireland M. J., Howard A. W., Huber D., 2016, ApJ, 817, 80
- Durisen R. H., Boss A. P., Mayer L., Nelson A. F., Quinn T., Rice W. K. M., 2007, in Reipurth B., Jewitt D., Keil K., eds, Protostars and Planets V. Univ. Arizona Press, Tucson, AZ, p. 607
- Enoch M. L., Corder S., Dunham M. M., Duchêne G., 2009, ApJ, 707, 103

- Evans N. J., II et al., 2009, *ApJS*, 181, 321
 Faherty J. K., Burgasser A. J., Cruz K. L., Shara M. M., Walter F. M., Gelino C. R., 2009, *AJ*, 137, 1
 Forgan D., Rice K., 2010, *MNRAS*, 406, 2549
 Forgan D., Rice K., 2011, *MNRAS*, 417, 1928
 Galicher R. et al., 2014, *A&A*, 565, L4
 Gammie C. F., 2001, *ApJ*, 553, 174
 Green J. D. et al., 2011, *ApJ*, 731, L25
 Greene T. P., Aspin C., Reipurth B., 2008, *AJ*, 135, 1421
 Gressel O., Turner N. J., Nelson R. P., McNally C. P., 2015, *ApJ*, 801, 84
 Guszejnov D., Krumholz M. R., Hopkins P. F., 2016, *MNRAS*, 458, 673
 Hao W., Kouwenhoven M. B. N., Spurzem R., 2013, *MNRAS*, 433, 867
 Hartmann L., Kenyon S. J., 1985, *ApJ*, 299, 462
 Hartmann L., Kenyon S. J., 1996, *ARA&A*, 34, 207
 Herbig G. H., 1977, *ApJ*, 217, 693
 Hubber D. A., Whitworth A. P., 2005, *A&A*, 437, 113
 Hubber D. et al., 2011a, Astrophysics Source Code Library, record ascl: 1102.010
 Hubber D. A., Batty C. P., Mcleod A., Whitworth A. P., 2011b, *A&A*, 529, A27
 Hubber D. A., Walch S., Whitworth A. P., 2013, *MNRAS*, 430, 3261
 Ireland M. J., Kraus A. L., Martinache F., Law N., Hillenbrand L. A., 2011, *ApJ*, 726, 113
 Johnson B. M., Gammie C. F., 2003, *ApJ*, 597, 131
 Kellogg K., Metchev S., Gagné J., Faherty J., 2016, *ApJ*, 821, L15
 Kenyon S. J., Hartmann L., 1987, *ApJ*, 323, 714
 Kenyon S. J., Hartmann L. W., Strom K. M., Strom S. E., 1990, *AJ*, 99, 869
 King A. R., Pringle J. E., Livio M., 2007, *MNRAS*, 376, 1740
 Kratter K. M., Lodato G., 2016, *ARA&A*, 54, 271
 Kratter K. M., Matzner C. D., 2006, *MNRAS*, 373, 1563
 Kratter K. M., Matzner C. D., Krumholz M. R., Klein R. I., 2010a, *ApJ*, 708, 1585
 Kratter K. M., Murray-Clay R. A., Youdin A. N., 2010b, *ApJ*, 710, 1375
 Kraus A. L., Ireland M. J., Martinache F., Lloyd J. P., 2008, *ApJ*, 679, 762
 Kraus A. L., Ireland M. J., Cieza L. A., Hinkley S., Dupuy T. J., Bowler B. P., Liu M. C., 2014, *ApJ*, 781, 20
 Krumholz M. R., 2006, *ApJ*, 641, L45
 Krumholz M. R., Burkert A., 2010, *ApJ*, 724, 895
 Kuzuhabara M., Tamura M., Ishii M., Kudo T., Nishiyama S., Kandori R., 2011, *AJ*, 141, 119
 Kuzuhabara M. et al., 2013, *ApJ*, 774, 11
 Laplace P. S., 1796, *Exposition du Système du Monde*, Imprimerie du Cercle-Social, Paris
 Li Y., Kouwenhoven M. B. N., Stamatellos D., Goodwin S. P., 2015, *ApJ*, 805, 116
 Li Y., Kouwenhoven M. B. N., Stamatellos D., Goodwin S. P., 2016, preprint ([arXiv:1609.00120](https://arxiv.org/abs/1609.00120))
 Lin D. N. C., Pringle J. E., 1990, *ApJ*, 358, 515
 Lin D. N. C., Faulkner J., Papaloizou J., 1985, *MNRAS*, 212, 105
 Lissauer J. J., 1993, *ARA&A*, 31, 129
 Liu Y. et al., 2015, *A&A*, 573, A63
 Liu H. B. et al., 2016, *Sci. Adv.*, 2, e1500875
 Lodato G., Clarke C. J., 2011, *MNRAS*, 413, 2735
 Lomax O., Whitworth A. P., Hubber D. A., Stamatellos D., Walch S., 2014, *MNRAS*, 439, 3039
 Lomax O., Whitworth A. P., Hubber D. A., Stamatellos D., Walch S., 2015, *MNRAS*, 447, 1550
 Low C., Lynden-Bell D., 1976, *MNRAS*, 176, 367
 Machida M. N., Inutsuka S.-I., Matsumoto T., 2006, *ApJ*, 649, L129
 Machida M. N., Inutsuka S., Matsumoto T., 2011, *ApJ*, 729, 42
 Macintosh B. et al., 2015, *Science*, 350, 64
 Makino J., Aarseth S. J., 1992, *PASJ*, 44, 141
 Marois C., Macintosh B., Barman T., Zuckerman B., Song I., Patience J., Lafrenière D., Doyon R., 2008, *Science*, 322, 1348
 Masunaga H., Inutsuka S., 2000, *ApJ*, 531, 350
 Matzner C. D., Levin Y., 2005, *ApJ*, 628, 817
 Meru F., Bate M. R., 2011, *MNRAS*, 411, L1
 Naud M.-E. et al., 2014, *ApJ*, 787, 5
 Nayakshin S., Cha S.-H., 2013, *MNRAS*, 435, 2099
 Nelson A. F., 2006, *MNRAS*, 373, 1039
 Offner S. S. R., Klein R. I., McKee C. F., Krumholz M. R., 2009, *ApJ*, 703, 131
 Offner S. S. R., Kratter K. M., Matzner C. D., Krumholz M. R., Klein R. I., 2010, *ApJ*, 725, 1485
 Paardekooper S.-J., Baruteau C., Meru F., 2011, *MNRAS*, 416, L65
 Palla F., Stahler S. W., 1993, *ApJ*, 418, 414
 Peneva S. P., Semkov E. H., Munari U., Birkle K., 2010, *A&A*, 515, 24
 Price D. J., 2007, *Publ. Astron. Soc. Aust.*, 24, 159
 Rameau J. et al., 2013, *ApJ*, 772, L15
 Rees M. J., 1976, *MNRAS*, 176, 483
 Rice W. K. M., Armitage P. J., Bate M. R., Bonnell I. A., 2003a, *MNRAS*, 339, 1025
 Rice W. K. M., Armitage P. J., Bonnell I. A., Bate M. R., Jeffers S. V., Vine S. G., 2003b, *MNRAS*, 346, L36
 Rice W. K. M., Lodato G., Armitage P. J., 2005, *MNRAS*, 364, L56
 Rice W. K. M., Forgan D. H., Armitage P. J., 2012, *MNRAS*, 420, 1640
 Rogers P. D., Wadsley J., 2012, *MNRAS*, 423, 1896
 Sallum S. et al., 2015, *Nature*, 527, 342
 Scholz A., Froebrich D., Wood K., 2013, *MNRAS*, 430, 2910
 Shakura N. I., Sunyaev R. A., 1973, *A&A*, 24, 337
 Spiegel D. S., Burrows A., Milsom J. A., 2011, *ApJ*, 727, 57
 Stamatellos D., 2015, *ApJ*, 810, L11
 Stamatellos D., Herczeg G. J., 2015, *MNRAS*, 449, 3432
 Stamatellos D., Whitworth A. P., 2008, *A&A*, 480, 879
 Stamatellos D., Whitworth A. P., 2009a, *MNRAS*, 392, 413
 Stamatellos D., Whitworth A. P., 2009b, *MNRAS*, 400, 1563
 Stamatellos D., Hubber D. A., Whitworth A. P., 2007a, *MNRAS*, 382, L30
 Stamatellos D., Whitworth A. P., Bisbas T., Goodwin S., 2007b, *A&A*, 475, 37
 Stamatellos D., Maury A., Whitworth A., André P., 2011a, *MNRAS*, 413, 1787
 Stamatellos D., Whitworth A. P., Hubber D. A., 2011b, *ApJ*, 730, 32
 Stamatellos D., Whitworth A. P., Hubber D. A., 2012, *MNRAS*, 427, 1182
 Terebey S., Shu F. H., Cassen P., 1984, *ApJ*, 286, 529
 Tobin J. J. et al., 2013, *ApJ*, 779, 93
 Tobin J. J. et al., 2016, *ApJ*, 818, 73
 Tomida K., Tomisaka K., Matsumoto T., Hori Y., Okuzumi S., Machida M. N., Saigo K., 2013, *ApJ*, 763, 6
 Toomre A., 1964, *ApJ*, 139, 1217
 Tsukamoto Y., Machida M. N., Inutsuka S.-I., 2013, *MNRAS*, 436, 1667
 Tsukamoto Y., Takahashi S. Z., Machida M. N., Inutsuka S., 2015, *MNRAS*, 446, 1175
 van der Plas G. et al., 2016, *ApJ*, 819, 102
 Vaytet N., Chabrier G., Audit E., Commerçon B., Masson J., Ferguson J., Delahaye F., 2013, *A&A*, 557, A90
 Vorobyov E. I., 2013, *A&A*, 552, A129
 Vorobyov E. I., 2016, *A&A*, 590, A115
 Vorobyov E. I., Basu S., 2005, *ApJ*, 633, L137
 Vorobyov E. I., Basu S., 2015, *ApJ*, 805, 115
 Whitworth A. P., Stamatellos D., 2006, *A&A*, 458, 817
 Zapatero-Osorio M. R., Béjar V. J. S., Martín E. L., Rebolo R., Navascués D. B. Y., Bailer-Jones C. A. L., Mundt R., 2000, *Science*, 290, 103
 Zhu Z., Hartmann L., Calvet N., Hernandez J., Muzerolle J., Tannirkulam A.-K., 2007, *ApJ*, 669, 483
 Zhu Z., Hartmann L., Gammie C., 2009a, *ApJ*, 694, 1045
 Zhu Z., Hartmann L., Gammie C., McKinney J. C., 2009b, *ApJ*, 701, 620
 Zhu Z., Hartmann L., Gammie C. F., Book L. G., Simon J. B., Engelhard E., 2010, *ApJ*, 713, 1134
 Zhu Z., Hartmann L., Nelson R. P., Gammie C. F., 2012, *ApJ*, 746, 110

This paper has been typeset from a *TeX/LaTeX* file prepared by the author.